nature astronomy

Article

https://doi.org/10.1038/s41550-026-02917-3

Primary evaporite in southern Utopia Planitia on Mars from Zhurong rover observations

Received: 7 April 2023

Accepted: 9 June 2026

Published online: 29 July 2026

Check for updates

Jiacheng Liu [1,2] ✉, Bo Wu [3], Wenyuan Gao [4], James W. Head III [2], Joseph R. Michalski [5,6] ✉, Mei-Fu Zhou [7], Anthony E. Williams-Jones [8], Xingao Hou [1], Zongcheng Ling [9,10], Zhongchen Wu [9], Changqing Liu [9], Yuqi Qian [1], Honglei Lin [11], Sen Hu [11], Yu Sun [12], Wei Tan [13,14], Xiao Wang [1] ✉ & Guochun Zhao [1,15]

The Zhurong rover has identified a layer consisting of platy rocks enriched in hydrous minerals on a ~0.76-Ga surface in southern Utopia Planitia, indicating unexpected recent aqueous activity on Mars. The exact type of these hydrous minerals has remained uncertain, inhibiting our understanding of the aqueous processes and potential habitability on recent Mars. Here we document unique decimetre-scale crystal morphologies observed by the Zhurong rover within the 5–10-cm-thick surface layer, indicative of euhedral selenite, a distinctive variety of gypsum. We interpret it as a signature of primary evaporite, distinct from previously identified sulfate deposits on Mars, which can only form in the presence of surface water with a cumulative water-equivalent column over time of at least 6.25–25 m. This cumulative thickness could have been achieved by either sustained or episodic upwelling of saline groundwater driven by magmatic activity into a very shallow, mostly ice-covered surface water body, whereas at any given time the actual liquid water layer would probably have been on the order of a metre or less. The large crystals of gypsum var. selenite are likely to contain abundant fluid inclusions—microscale pockets of ancient brine that could provide a unique window into the geochemical and potentially even biological environment of the Martian subsurface during the Amazonian period.

Although the prevailing consensus holds that Mars has remained predominantly cold and icy throughout the Amazonian period[1] (from approximately 3 billion years ago (Ga) to the present), the Zhurong rover's discovery of hydrous minerals[2–4] on a geologically young surface (~757 ± 66 million years ago (Ma))[5] in southern Utopia Planitia suggests recent surface aqueous activity on Mars. This unexpected finding challenges current paradigms regarding the evolution of Martian climate and aqueous processes[2]. While the presence of hydrous minerals is strongly supported by OH/H_2O spectral absorptions[2,4] and direct detection of volatiles[6,7], the specific type and formation mechanism of primary hydrous mineral have remained ambiguous, with sulfates, silica and allophane all considered likely candidates[2–4]. This uncertainty restricts our full understanding of Martian aqueous processes and the planet's potential to have sustained habitable environments during the Amazonian period.

Our study presents a detailed investigation of the platy rocks enriched in hydrous minerals, with particular emphasis on the crystal habits observed in situ. Integrating mineralogical, spectral and

A full list of affiliations appears at the end of the paper. ✉e-mail: jcliu01@hku.hk; jmichal@hku.hk; wangfuyu@hku.hk

 https://doi.org/10.1038/s41550-026-02917-3

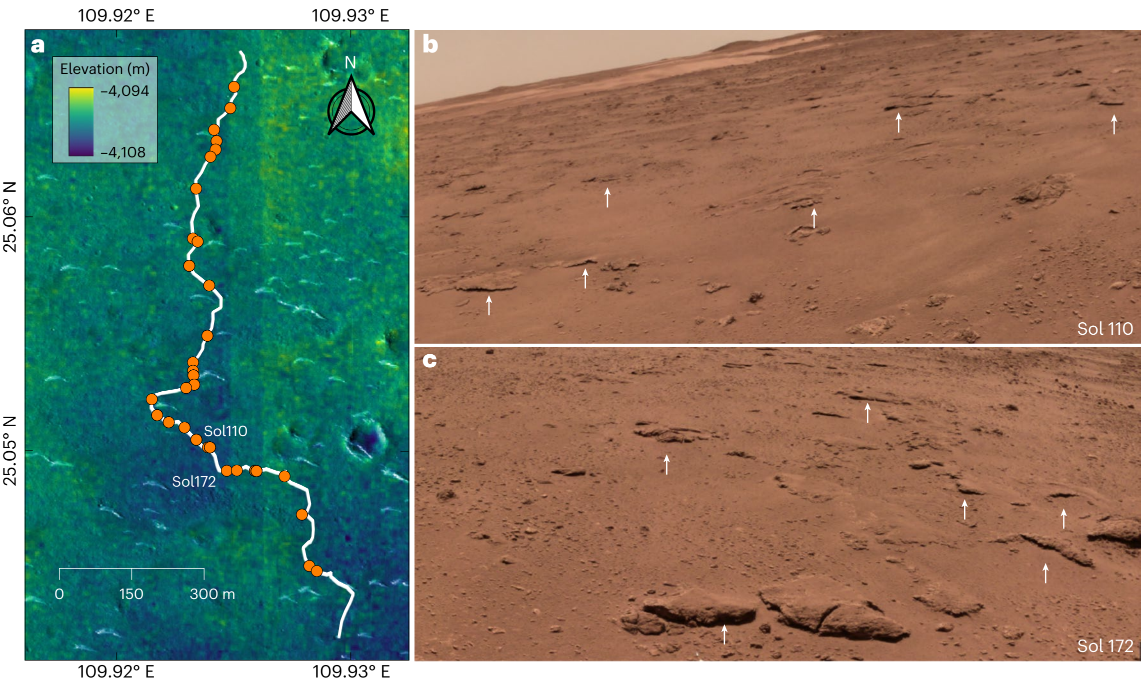

Fig. 1 | A layer consisting of platy rocks rich in hydrous mineral at the surface of the Zhurong landing site. a, The traverse of the Zhurong rover, with the detection of platy rocks denoted by orange circles. **b**,**c**, Hydrous mineral-rich platy rocks (indicated by the white arrows) captured at different locations and times along the traverse (Sol 110 (**b**); Sol 172 (**c**)), define an originally laterally continuous layer approximately 5–10 cm thick, as seen in the NaTeCams images.

compositional data, we identify the primary hydrous mineral at the Zhurong landing site as decimetre-scale euhedral selenite, a distinctive variety of gypsum. This gypsum var. selenite constitutes a layer of primary evaporite, distinguished from previously reported Martian sulfates by its Amazonian age, macroscopic crystal morphology and inferred geological formation processes. The identification of a primary evaporite layer not only provides compelling evidence for the existence of surface water during the Amazonian period but also has important implications for strategies aimed at searching for potential Martian biosignatures.

Gypsum var. selenite discovered by the Zhurong rover

During its traverse (Fig. 1a), the Zhurong rover revealed an extensive bright-toned surface layer consisting of platy rocks on the surface of southern Utopia Planitia (Fig. 1b,c and Extended Data Fig. 1), characterized by a high abundance of hydrous minerals[2,3]. These exposures seems to define an originally laterally continuous layer approximately 5–10 cm thick (Fig. 1b,c), although its broader continuity cannot be established from the available images alone.

Although many of the platy rocks were initially mantled by sand (Extended Data Fig. 1), close examination of freshly exposed surfaces reveals a homogeneous interior, displaying uniform texture and colour (Fig. 2a–c). This internal consistency, coupled with the angular morphology, which are manifested as sharp-edged, blade-like and faceted fragments rather than rounded chips (Extended Data Fig. 2), suggests that the platy rocks consist of tightly packed crystal clusters. The absence of spheroidal weathering features (Fig. 1 and Extended Data Fig. 2) contrasts with the expectation given the intense recent aeolian activity inferred from widespread dunes in the region[8] (Fig. 1a and Extended Data Fig. 1). Instead, the prevalence of angular surfaces points to a structure governed primarily by the internal texture, such as crystal habit, rather than exogenic erosional forces, although aeolian abrasion probably facilitated the exposure of the internal structure.

The crystal clusters predominantly exhibit a radiating architecture, characterized by upward-curving forms (cabbage-like forms, sometimes termed 'cavoli' in the Italian literature) and sutured crystal termini (Fig. 2a–c), closely resembling those of terrestrial gypsum var. selenite[9,10] (Fig. 2d–f). Individual tabular crystals within these clusters measure approximately 5–10 cm in length and 0.2 cm in thickness (Fig. 2b,c and Extended Data Fig. 3). Remarkably, we observe a distinct Christmas-tree morphology (Fig. 3a–c), featuring acute downward-pointing angles and widths ranging from 0.5 cm to 5 cm. The crystal twin tails are thicker than their bases (Figs. 2a–c and 3c), a feature characteristic of fishbone twinned gypsum var. selenite[9,10] (Fig. 3d–f). Intercrystalline spaces observed between twins, probably enlarged by aeolian abrasion (Fig. 3c), suggest a low hardness of these crystals. The physical properties and crystal habits—high reflectance, large crystal size, low hardness, radiating clusters and fishbone twinning—all point to gypsum var. selenite[9–12] (Figs. 2 and 3). There are two common varieties of gypsum that form large crystals: selenite and satin spar, which are often mislabeled. The gypsum observed here is clearly selenite rather than satin spar, as satin spar typically appears in parallel fibrous aggregates, whereas selenite is characterized by fishbone twinning or radiating clusters (Figs. 2 and 3).

In addition, this mineralogical interpretation is strongly corroborated by spectral and compositional analyses via the Mars Surface Composition Detector (MarSCoDe). The reflectance spectra of the platy rocks display relatively notable spectral absorptions at ~1.45 µm (~3%), ~1.95 µm (~10%) and ~2.20–2.25 µm (~5%), and weaker absorptions at ~1.20 µm and ~1.75 µm (Extended Data Fig. 4 and 5)[2,3]. The relatively strong absorptions at ~1.45 µm, ~1.95 µm and ~2.20–2.25 µm could be attributed to hydrated sulfates, hydrated silica and/or allophane[2–4]. However, the weak absorptions at ~1.21 and ~1.75 µm are more consistent with the presence of gypsum[3]. Chemically, the principal constituents of gypsum ($CaSO_4{\cdot}2H_2O$)—namely S, H and Ca—are clearly detected[4,6,7] by MarSCoDe laser-induced breakdown spectroscopy (LIBS). The diagnostic peaks closely match those of the onboard gypsum reference target (Extended Data Figs. 6–8). More importantly,

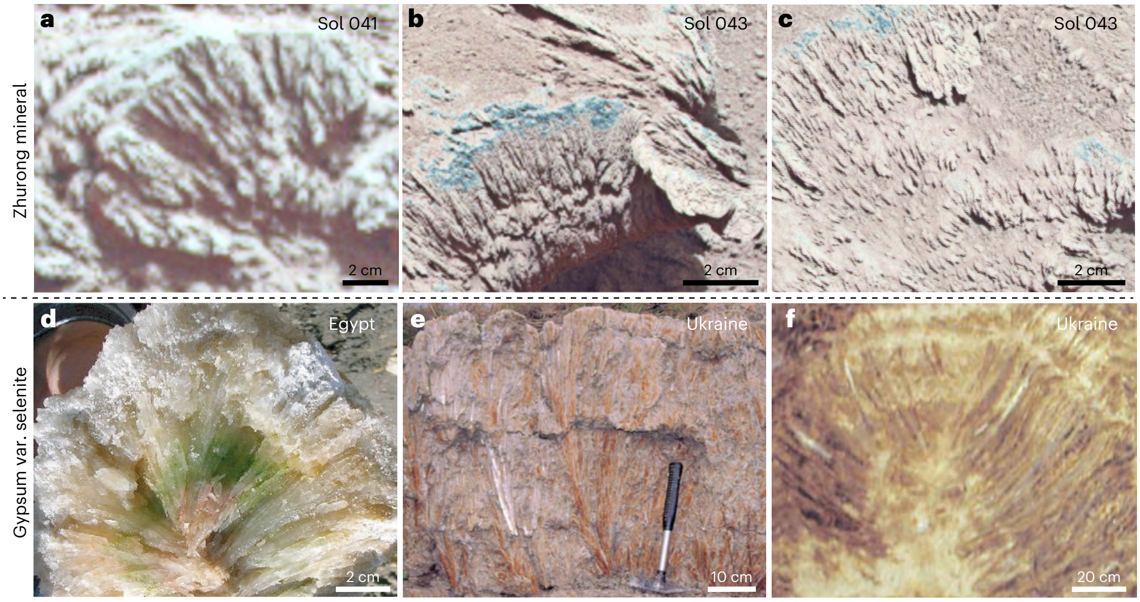

Fig. 2 | The interior radiative structure of platy rocks, analogous to crystal clusters of terrestrial gypsum var. selenite. a–**c**, Upward-radiating clusters of hydrous mineral crystals with sutured ends, captured at different locations and times along the traverse (Sol 041 (**a**); Sol 043 (**b**,**c**)) by the MSCam. The crystal clusters in **b** and **c**, which are observed at different positions during the same Sol, are composed of tabular crystals exhibiting ~2 mm thickness and up to 10 cm in planar dimension. **d**, A palm-like pattern of upward-grown selenite crystals from EMISAL (The Egyptian Minerals & Salts Co.), Egypt[9], resembling the crystal cluster in **a** observed by Zhurong. **e**, A fanning cluster of gypsum var. selenite, found in Holovchyntsi, Ukraine[10], similar to the crystal cluster in **b** observed by Zhurong. **f**, Gypsum var. selenite domes with subparallel crystals curved upwards, located in Krystalna Cave, Zal Hlyb, Kryvche, Ukraine[10]. Panel **d** adapted from ref. 9, under a Creative Commons license CC BY-SA 4.0. Panels **e** and **f** reproduced with permission from ref. 10, Acta Geologica Polonica.

there is a strong positive correlation between Ca and S, providing compelling compositional evidence for the presence of Ca sulfates[7] (Extended Data Fig. 9). Positive correlations can also be found between S and H, although an outlier with higher H and Si signals is present[6]. It is possible that other phases, such as hydrated amorphous materials, may also contribute to the hydration signature[4,7]. Synthesizing the physical, textural, spectral and compositional observations, we conclude with high confidence that the primary hydrous mineral in the platy rocks is decimetre-scale gypsum var. selenite.

The gypsum var. selenite identified by Zhurong constitutes a laterally extensive, approximately 5–10-cm-thick layer (Fig. 1) of macroscopic, euhedral crystals deposited on a geologically young Amazonian surface (~757 ± 66 Ma)[5]. Spectral homogeneity across all analysed samples (Extended Data Fig. 5) attests to the mineralogical uniformity of this surface layer consisting of platy rocks. The distinct, homogeneous nature and large crystal sizes confirm that this deposit represents a primary evaporite layer rather than the diagenetic crystals found elsewhere on Mars. The presence of patchy weathering suggests moderate physical alteration, probably resulting from ongoing aeolian erosion[8].

Gypsum typically forms through chemical precipitation in neutral to slightly acidic environments via evaporation[11]. The gypsum var. selenite discovered by Zhurong is exceptional in its large crystal dimensions, well-developed selenite twinning and pronounced curvature of crystal clusters. These crystal habits provide valuable constraints on the palaeoenvironments, including solution chemistry, supersaturation and evaporation or freezing rates. First, the formation of such large crystals generally reflects growth under moderate supersaturation and low nucleation density, favouring enlargement of individual crystals over rapid precipitation of numerous small nuclei[13]. Second, the observed curvature of crystal clusters probably arises from homoepitaxial growth, wherein successive layers or crystals accrete with slight angular misalignments—a process typically associated with high evaporation rates[14]. Third, the presence of twinned crystals indicates conditions in which the parent brine attained sufficient supersaturation to overcome the higher activation energy required for twinning, facilitating the development of these distinctive structures[14].

The origin of the gypsum var. selenite

Sulfates are widespread across the Martian surface[15], yet most sulfates investigated by previous rovers—such as Opportunity at Meridiani, Curiosity in Gale crater and Perseverance in Jezero crater—are typically amorphous or fine-grained, or occur as diagenetic fracture fills and disseminated cements[16–18]. By stark contrast, the Zhurong rover discovered a laterally extensive, layered deposit of large, euhedral gypsum var. selenite in southern Utopia Planitia. This unique occurrence points to a fundamentally different surface aqueous environment in this region compared with other Martian localities.

Such large, euhedral gypsum var. selenite crystals arranged in a continuous layer are unlikely to be formed by direct groundwater evaporation within microfractures or capillary rise and subsequent evaporation of groundwater within sediments. Specifically, groundwater evaporation within fractures that connect to the surface yield crystalline sulfates as fracture fills or veins[19]. Capillary rise and subsequent evaporation of saline groundwater[2] more typically produces nodules within sandy sediments or gypsum 'desert roses', which occur as rosette-like aggregates containing abundant included sand grains. The macroscopic crystal habit, size and layered geometry of the Zhurong gypsum (var. selenite) are entirely different from those described above, but more consistent with precipitation at or near the bottom of a shallow, ponded body of surface water, in which $CaSO_4$-rich brines were sustained for sufficient time to allow the growth of large, euhedral selenite crystals.

By analogy to terrestrial settings, primary evaporite layers typically form by the evaporation of standing bodies of surface water, such as palaeolakes or marine shorelines[9]. At the Zhurong landing site, the geomorphological context—a broad, open, gently sloping surface lacking fluvial or closed-basin features[20]—makes a long-lived, topographically closed, open-water lake unlikely. Instead, the hypothesis that the deposit represents an evaporite formed from a palaeo-ocean

https://doi.org/10.1038/s41550-026-02917-3

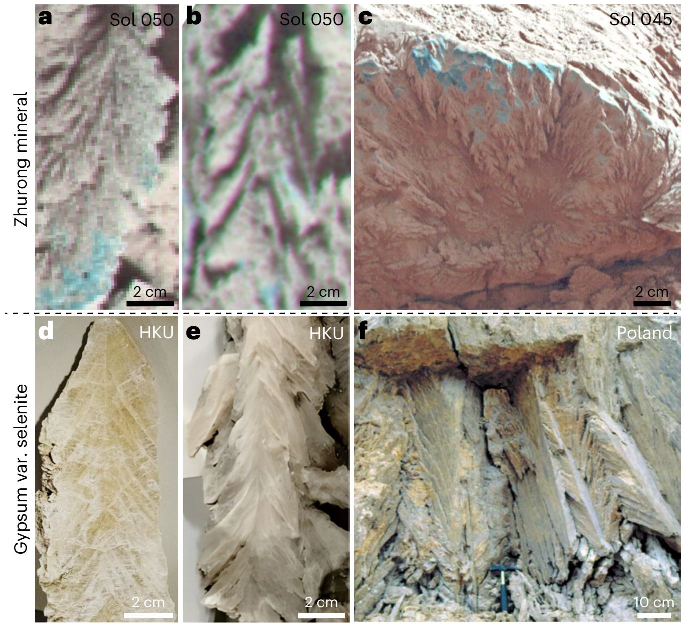

Fig. 3 | The Christmas-tree morphology of hydrous mineral crystal akin to the fishbone crystal twinning of gypsum var. selenite. **a**,**b**,**d**,**e**, Close-up views of the Christmas-tree morphologies of the crystal (**a** and **b**), closely resembling the reference fishbone crystal twinning of gypsum var. selenite exhibited in the Stephen Hui Geological Museum of The University of Hong Kong (HKU; **d** and **e**, respectively). **c**,**f**, A crystal cluster in the MSCam image featuring many small 'Christmas trees' (**c**), similar to the giant gypsum var. selenite intergrowths at Leszcze quarry, Nida area, Poland[10] (**f**). The large intercrystalline spacings in **c** may result from aeolian abrasion. The progressively increased spacing from **a** to **c** suggests an increasing degree of aeolian abrasion. Panel **f** reproduced with permission from ref. 10, Acta Geologica Polonica.

is plausible, as geomorphic observations suggest the landing site lies within an ancient shoreline environment[21]. However, it faces a substantial challenge given the young age of the primary evaporite.

The broader Zhurong region has a late Hesperian model age of ~3.23 (+0.15/−0.47) Ga (ref. 5), consistent with emplacement of the Vastitas Borealis Formation as the regional substrate. By contrast, Zhao et al. (2021) obtained a much younger late Amazonian age of 757 (±66) Ma from the population of smaller craters (≤1 km) within and around the landing ellipse[5]. This raises a challenge for the palaeo-ocean hypothesis: the Zhurong gypsum var. selenite is situated on a surface dated to 757 (±66) Ma (ref. 5), a period typically characterized by an icy and arid climate on Mars[22], which is unlikely to sustain an ocean. One could argue that the deposit represents an exhumed remnant of subsurface Hesperian marine sedimentary layers exposed by erosion[23] and that the young age (757 ± 66 Ma) might have resulted from the erosion of the indurated sedimentary rock and the mantling of the surface by a lag deposit and aeolian materials, similar to what has occurred at Meridiani Planum[24]. However, several lines of evidence argue against the ~0.76-Ga age being solely an erosional resetting age imposed on late Hesperian bedrock. First, the unconsolidated sand mantle is thin (less than or approximately a few metres)[25], and there is no indication of tens to hundreds of metres of the Amazonian deflation or burial of the platy unit. Second, aeolian dunes at the site are morphologically fresh and probably have crater retention ages around 1 Ma (ref. 8), much younger than 757 (±66) Ma, indicating that the dune system represents a superposed, very recent process that cannot by itself account for the much older resurfacing age. Third, the platy evaporite bearing unit, which directly exposed beneath this thin sand mantle (Extended Data Fig. 1a), lacks a protective layered overburden (Fig. 1b,c) suggestive of exposure of ancient rocks by exhumation but exhibits textures and geometries consistent with surface deposition. We therefore favour an interpretation in which the 757 (±66) Ma age marks a Amazonian episode of resurfacing that involved emplacement of loose materials and the formation of the primary evaporite at or near the surface. In this scenario, the Vastitas Borealis Formation forms the older regional substrate (~3.23 Ga)[5], while the evaporite forming event represents a younger (~0.76 Ga) aqueous episode superposed upon it[2].

Reconciling the existence of Amazonian-age evaporites with the prevailing understanding of a cold, icy climate during this period[1] is challenging, as any surface water would have existed mainly as ice rather than liquid. This necessitates an alternative formation scenario for the Zhurong primary evaporite.

It has long been hypothesized that substantial volatiles—both surface/ground ice and subsurface groundwater—persisted in the northern lowlands during the Amazonian period[26–28]. Notably, the Utopia Planitia displays a suite of geomorphological features associated with volatile-rich processes, such as sedimentary volcanoes[29] (Extended Data Fig. 10a,b), troughs (Extended Data Fig. 10a,c), maars[30], ghost craters and mega-lahars[26,31,32]. The widespread sedimentary volcanoes[29] indicate eruptions of deep-seated materials, including fine sediments and groundwater[33]. Intriguingly, the ages of the isolated mud volcanoes (~760 ± 200 Ma)[34] and the resurfacing age of the landing site itself (~757 ± 66 Ma)[5] are consistent, suggesting a spatial and temporal link between primary evaporite formation and mud volcanism. The fine-grained materials carried by upwelled groundwater would have gradually settled to the bottom of the water column, forming a loose surface layer[25] capable of burying small craters that have been partly erased, and yielding an apparently young surface age. This mechanism may also explain the exceptionally smooth and flat morphology of the Zhurong landing region. Theoretically, the evaporation and/or freezing of saline water brought to the surface by such eruptions could produce evaporite deposits.

Additional geomorphological evidence points to a substantial magmatic event: the region is cut by widespread dikes[29,35] (Extended Data Fig. 10c) and lies relatively close to the Elysium volcanic province[34] and its inferred active mantle plume[36]. Prolonged persistence of ground and surface ice would have brought it into contact with intruding magma[30]. The resultant thermal input could have triggered extensive melting of ground and surface ice and subsequent collapse of overlying rocks. The pressure caused by collapse could have upwelled abundant groundwater and dissolved ions to the surface, establishing conditions conducive to evaporite precipitation.

To further evaluate the feasibility of forming a 5–10-cm-thick primary evaporite, a mass balance calculation is essential to determine whether sufficient dissolved ions could have been supplied. Martian groundwater during the Amazonian period probably had elevated salinity because of the high sulfur concentration in Martian crust[37] and a progressively desiccating and cooling climate[38]. The decreasing temperature (0–40 °C) can only modestly decrease the solubility of gypsum (on the order of tens of per cent over this range)[39]. However, this high ionic content, especially in the presence of Mg—which could be common in Martian groundwater owing to alteration of olivine—would have substantially improved gypsum solubility (up to 0.8 wt%)[40]. High salinity (0.4–0.8 wt%) of groundwater was possible if the groundwater was equilibrated with a deep gypsum layer[41]. Head and Wilson (2007)[42] predicted the existence of such salt layers in the Vastitas Borealis Formation (Fig. 4a), which precipitated from the Hesperian ocean. At this salinity of 0.8 wt%, the deposition of a 5–10-cm-thick evaporite layer would require that the system process a cumulative water equivalent column of approximately 6.25–12.5 m of $CaSO_4$-bearing brine. If the dissolved gypsum was 0.4 wt%, half of the gypsum solubility, the required cumulative water equivalent thickness would be 12.5–25 m. Importantly, this 6.25–25 m value does not imply that a single, open body of water of that depth existed at one time. Rather, it can be achieved by sustained or repeated upwelling of saline groundwater into a shallow

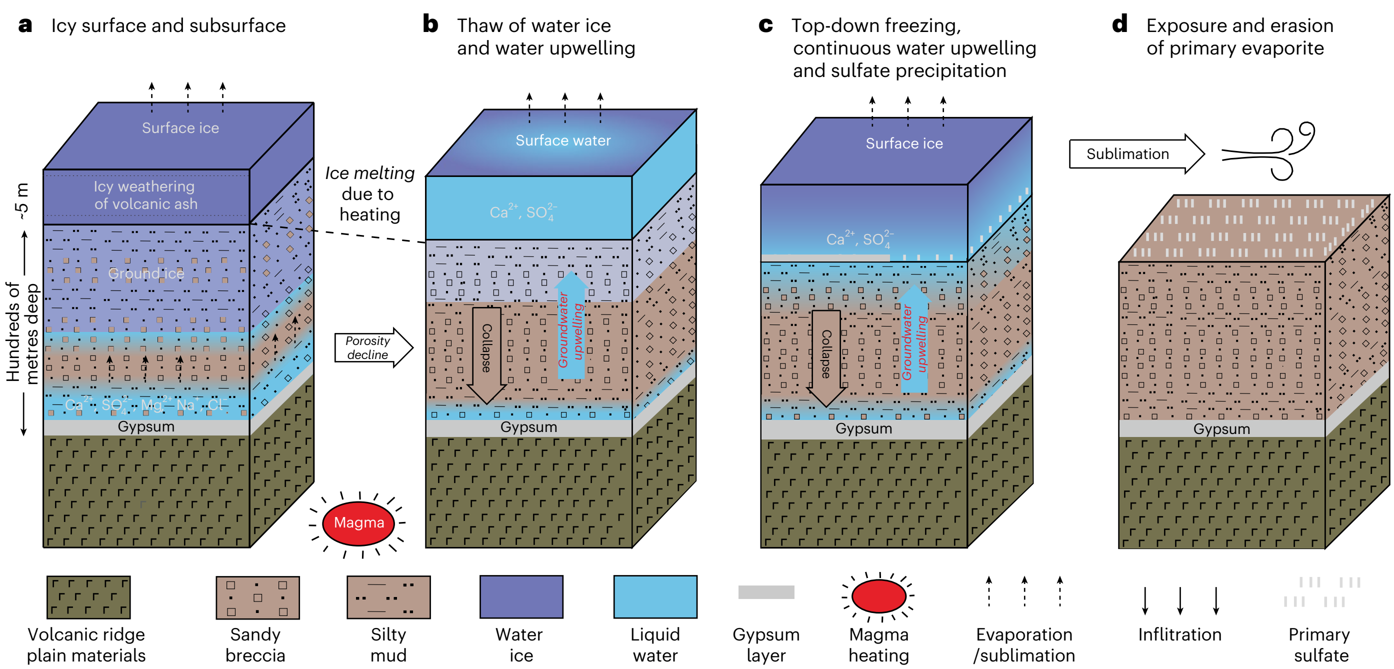

Fig. 4 | A conceptual formation mechanism of Zhurong primary evaporite. **a**, The prolonged existence of surface and ground ice, and groundwater equilibrated with deep gypsum, and its interaction with magma. **b**, Magma-induced melting of ground and surface ice, resulting in reduced porosity, surface collapse and upwelling of groundwater to surface. A parallel branch, not shown, could involve dike-released groundwater, which would then follow the same pathways outlined in **c** and **d**. **c**, Rapid cooling at the surface leads to fast top-down freezing, forming a thin ice lid and a shallow (metre-scale) sub-ice brine lens rather than a deep, long-lived open lake. Continued magmatic heating from below maintained the basal brine layer liquid beneath the ice lid, while the ice exposed at the surface was continuously removed by sublimation under the low-pressure Martian atmosphere. Newly supplied warm brine froze at the top to replenish the ice lid, and sublimation steadily removed water from the system, progressively cryoconcentrating the underlying brine. Under these conditions, sulfates precipitated as primary evaporites (gypsum var. selenite) at or near the bottom of the shallow, ice-covered water body. **d**, As magmatic activity waned and groundwater supply diminished, the remaining brine ultimately froze and the surface ice completely sublimed away, leaving the primary sulfate unit exposed on the surface. Subsequent aeolian erosion and deflation partially reworked and exposed the evaporite layer.

(probably metre scale), mostly ice-covered pond, where brine was confined and progressively concentrated by freezing and sublimation.

The small local relief (≲10–14 m) and gentle regional slope at the Zhurong site therefore do not preclude such a system, because lateral confinement is provided primarily by freezing and low-permeability frozen ground, rather than by a topographically closed basin. In this configuration, the actual liquid water depth at any given time can remain small (metre scale), while the integrated volume of upwelling brine over the duration of activity corresponds to a cumulative water equivalent thickness of 6.25–25 m. The cumulative water depth charged by the release of groundwater could be roughly estimated by the collapse depth of the region. The collapse features such as troughs and ghost craters in the region could be up to 100 m deep[43]. Therefore, the cumulative amount of groundwater upwelled to the surface alone could be sufficient to produce the primary evaporite with thickness of 5–10 cm. The selenite bearing platy unit observed by Zhurong is not necessarily located within these collapse structures. Here, the collapse features are used solely to illustrate the potential magnitude of cryosphere failure and groundwater/ice mobilization capable of supplying sufficient brine volumes on a regional scale, rather than as the immediate depositional sites of the gypsum var. selenite.

In addition to groundwater release, ice melting, facilitated by heating of magma and/or volanism[44], is consistent with the exposure of dike ridges (Extended Data Fig. 10c), which might have been the products of the solidified magma-filled cracks and interaction with surface ice[45]. The height of the exposed dike is several metres, implying that several metres of surface ice—possibly a latitude-dependent ice–dust mantle[27]—could have been converted into meltwater. Surface ice probably contained additional ions derived from atmospheric precipitation of volatiles (S and Cl) and air-fall sediments, such as volcanic ash[46]. Fine-grained materials, altered by sulfuric acid weathering, would have released Mg^{2+} and Ca^{2+} ions[47] into meltwater with the formation of amorphous materials[4].

In our preferred model, local magmatic activity and related dike intrusion episodically heated the cryosphere and underlying aquifers, causing warm, saline groundwater to ascend towards the surface. Upon reaching the cold near surface environment, the upper part of the water column froze almost immediately, forming an ice lid, while the basal portion remained liquid owing to continued magmatic heating from below. Throughout this stage, the surface ice was continuously removed by sublimation under the low-pressure Martian atmosphere during the Amazonian period. Freezing of newly supplied warm brine at the top replenished the ice lid, whereas sublimation steadily removed water from the system, leading to progressive cryoconcentration of the underlying brine. As long as magmatic heating and groundwater supply persisted, this sub-ice brine layer could remain liquid and highly concentrated for an extended period. Freezing would elevate salinity[42], driving $CaSO_4$ supersaturation—a cryoconcentration process analogous to intense evaporation in terrestrial evaporitic settings. The high rate of water removal from solution by efficient freezing promotes the growth of curved crystal clusters and characteristic twinned morphologies[48]. In addition, the presence of Mg^{2+} ions, probably abundant in Martian groundwater, could suppress nucleation and crystallization rates[40], favouring the development of large gypsum var. selenite crystals. Thus, freezing and sublimation under the icy climate during the Amazonian period could have produced a neutral, stable and progressively concentrated ionic environment, ideal for the unusual macrocrystalline gypsum growth observed. Preferential downward migration of the most soluble brines, enriched in chlorides (NaCl and $MgCl_2$) and magnesium sulfate, could explain the dominance of the less soluble gypsum in the preserved surface evaporite. Furthermore, the lack of carbonate could be explained by the limited interaction with the atmosphere owing to the freezing of most surface water[42].

In summary, geological context, climatic factors and mass balance calculations collectively support a formation scenario wherein the melting of surface and ground ice, coupled with the upwelling of ion-rich groundwater, led to the precipitation of the primary gypsum var. selenite evaporite observed by Zhurong.

The astrobiological significance of the primary gypsum var. selenite

Sulfates rank among the most important hydrous minerals on Mars[15], yet the gypsum var. selenite discovered at the Zhurong landing site stands apart from sulfate deposits documented elsewhere on the planet. In particular, the large crystals of gypsum var. selenite are likely to contain abundant fluid inclusions[49]—microscale pockets of ancient brine that are promising microenvironments for the entrapment and preservation of organic matter and potential biosignatures[50]. These inclusions could have sequestered materials from ancient groundwater, providing a unique window into the geochemical and perhaps even potential biological environment of the Martian subsurface[11]. If extant or extinct life ever inhabited the Martian subsurface, it is conceivable that evidence of such life—such as organic molecules or life-related elements—may be preserved within these inclusions.

Beyond acting as repositories for potential biosignatures, primary evaporites may have played an important protective role[51]. The surface materials at the Zhurong site have been exposed to harsh Martian surface conditions for hundreds of millions of years, including intense chemical oxidation, cosmic ray bombardment and ultraviolet (UV) radiation—all factors known to degrade organic matter[52,53]. Gypsum var. selenite can provide considerable protection against chemical oxidation, and its relatively high density offers partial shielding from cosmic rays[54]. However, a major challenge for the long-term preservation of organic matter within the gypsum is posed by UV radiation, as gypsum is relatively transparent to UV, especially in its uppermost layers over geological timescales[55]. Consequently, the capacity of these deposits to shield organic biosignatures from UV remains uncertain and warrants further experimental investigation.

The considerable thickness (up to 10 cm) and large crystal size of the gypsum var. selenite layer may have afforded some degree of protection to any organic matter encapsulated within, especially at greater depths where UV penetration is diminished. Nonetheless, it is likely that some organic biosignatures have been altered or decomposed due to prolonged exposure to surface radiation. Thus, quantitative assessments of the attenuation of UV and cosmic rays by gypsum var. selenite of comparable thickness and texture are critical for evaluating the potential survival of organic biosignatures. Even if primary organic molecules have decomposed, residual organic fragments or characteristic decomposition products may still be detectable within fluid inclusions, underscoring the importance of targeting such microenvironments in the search for life[54]. Understanding these preservation mechanisms could provide invaluable insights into the strategy to search for traces of life on Mars in future Mars sample return missions.

Methods

Detailed observations of the platy rocks were enabled by high-resolution imagery acquired by the Navigation and Terrain Cameras (NaTeCams) and the Multispectral Camera (MSCam) onboard the Zhurong rover. Compositional information for rocks and soils at the landing site was obtained via the MarSCoDe, which integrates a laser-induced breakdown spectrometer and a short-wave infrared (SWIR) spectrometer. All MarSCoDe datasets used in this study are publicly available through the Lunar and Planetary Data Release System (https://moon.bao.ac.cn/).

Topography and landforms

Geomorphological features were investigated using images from Tianwen-1's high-resolution camera (HiRIC), NASA's Mars Reconnaissance Orbiter (MRO) Context Imager (CTX, 6 m per pixel, https://murray-lab.caltech.edu/CTX/). The colour-coded topographic map of the Zhurong landing site was generated by coregistering regional digital image maps with digital elevation models derived from the HiRIC. The rover's traverse trajectory and identified stratified duricrust exposures were accurately mapped using geographic coordinates from the onboard NaTeCams. The elevation profile along the traverse was extracted from the HiRIC-based digital elevation models of the Zhurong landing site.

LIBS

This study utilizes the Level 2B dataset from MarSCoDe LIBS onboard the Zhurong rover, which is generated through radiometric calibration, dark background removal and averaging of 60 raw spectra for each target. This dataset comprises 19 rock targets, 11 soil targets and 10 dune targets, and it is available at CNSA's Lunar and Planetary Data Release System. However, only rock targets are used in this study, as they more accurately represent the bedrock composition. Before further data processing, the quality of all LIBS spectra is evaluated with a LIBS quality index (LQI) method from Chen et al.[56], and LIBS spectra with poor quality (LQI >3) are excluded to ensure identification of weak S peaks.

Data processing adopts the following steps: (1) denoising the spectra with a ChemCam-style undecimated wavelet transform method[57]; (2) calibrating the wavelength values considering both the onboard calibration target (Ti plate) and charge-coupled device temperature using the method of Zhang et al.[58]; and (3) removing the unwanted spectral continuum using asymmetric least squares. In detecting sulfur by LIBS, the ~564-nm emission peak is chosen as the identification signal because it is less likely to be affected by other elements[59]. It can be identified by determining the centroid position of the spectral peak following baseline correction. Reference spectra obtained from an MarSCoDe Calibration Target (MCCT) gypsum are also used as auxiliary standards in identifying S peaks. In addition, the Ca 612.4-nm line and the H 656.5-nm and C 658.1-nm double peaks are selected as identification markers for the corresponding elements, according to previous studies[7].

The analysis of selected peaks in LIBS spectra is based on peak fitting, with the voigt_profile function accessed from Python's scipy.special and the curve_fit function from scipy.optimize. After removing the baseline, the areas of the fitted peaks were calculated through integration. The area of the oxygen emission peak near 778 nm (comprising OI at 777.41, 777.63 and 777.75 nm, which together form a single peak) was used as the normalization denominator for the previously mentioned emission peaks. This approach was chosen because normalized emission areas have been shown to better correlate with element concentrations in plasma[59]. In addition, the correlations between sulfur and calcium, as well as sulfur and hydrogen, in the bedrock at the Zhurong landing site were assessed by calculating their R^2 values.

SWIR spectrometer

The released SWIR spectra have been processed to Level 2B, incorporating both dark current correction and absolute radiometric calibration. To address potential shifts in the centre wavelengths of the spectrometer channels after launch, spectral drift correction was applied using the pipeline described by Lin et al.[60].

The rover carries two onboard Spectralon calibration panels (Labsphere) with nominal reflectances of 99% and 40%. Before each target observation, the spectrometer recorded the radiance of one calibration panel. In this study, the 40% reflectance panel was used for reflectance retrieval. The target reflectance (Ref_{tar}) was calculated using the following equation[2]:

$$Ref_{tar} = \frac{Rad_{tar}}{Rad_{cal}} \times Ref_{cal}, \quad (1)$$

where Rad_{tar} and Rad_{cal} denote the radiance data of the observed target and calibration panel, respectively. Ref_{tar} and Ref_{cal} represent the reflectance of the target and calibration panel, respectively. The calibrated SWIR spectra are shown in Extended Data Figs. 3 and 4.

Data availability

The datasets analysed during the current study are publicly available. The Tianwen-1 Zhurong rover data are publicly available via the China National Space Administration (CNSA) Lunar and Planetary Data Release System at https://moon.bao.ac.cn/web/enmanager/zygj, which can be accessed via the following path: Home Page > Scientific Data > Mars. The Mars Reconnaissance Orbiter (MRO) Context Camera (CTX) image data are publicly available via the Bruce Murray Laboratory for Planetary Visualization at Caltech (https://murray-lab.caltech.edu/CTX/).

References

1. Diniega, S. & Smith, I. B. High-priority science questions identified at the Mars Workshop on Amazonian and Present-Day Climate. *Planet. Space Sci.* **182**, 104813 (2020).
2. Liu, Y. et al. Zhurong reveals recent aqueous activities in Utopia Planitia, Mars. *Sci. Adv.* **8**, eabn8555 (2022).
3. Lin, H. et al. Mineralogical evidence of water activity in the northern lowlands of Mars based on inflight-calibrated spectra from the Zhurong rover. *Sci. China Earth Sci.* **66**, 2463–2472 (2023).
4. Liu, C. et al. Aqueous alteration of the Vastitas Borealis Formation at the Tianwen-1 landing site. *Commun. Earth Environ.* **3**, 1–11 (2022).
5. Zhao, J. et al. Geological characteristics and targets of high scientific interest in the Zhurong landing region on Mars. *Geophys. Res. Lett.* **48**, e2021GL094903 (2021).
6. Zhao, Y.-Y. S. et al. In situ analysis of surface composition and meteorology at the Zhurong landing site on Mars. *Natl Sci. Rev.* **10**, nwad056 (2023).
7. Zhang, Y. et al. Volatile elements characterized by MarSCoDe in materials at Zhurong landing site. *Astron. J.* **168**, 150 (2024).
8. Gou, S. et al. Transverse aeolian ridges in the landing area of the Tianwen-1 Zhurong rover on Utopia Planitia. *Mars. Earth Planet. Sci. Lett.* **595**, 117764 (2022).
9. Ali-Bik, M. W., Metwally, H. I. M., Wali, A. M. A. & Kamel, M. G. Facies and geochemistry of non-marine gypsum, EMISAL, Egypt. *Geol. Acta* **11**, 409–422 (2013).
10. Babel, M. Selenite-gypsum microbialite facies and sedimentary evolution of the Badenian evaporite basin of the northern Carpathian Foredeep. *Acta Geol. Pol.* **55**, 187–210 (2005).
11. García-Ruiz, J. M., Villasuso, R., Ayora, C., Canals, A. & Otálora, F. Formation of natural gypsum megacrystals in Naica, Mexico. *Geology* **35**, 327–330 (2007).
12. Rodríguez-Aranda, J. P., Rouchy, J. M., Calvo, J. P., Ordóñez, S. & del Cura, M. A. G. Unusual twinning features in large primary gypsum crystals formed in salt lake conditions, Middle Miocene, Madrid Basin, Spain—palaeoenvironmental implications. *Sediment. Geol.* **95**, 123–132 (1995).
13. Reiss, A. G., Ganor, J. & Gavrieli, I. Size distribution and morphology of gypsum crystals precipitating from hypersaline solutions. *Cryst. Growth Des.* **19**, 6954–6962 (2019).
14. Aquilano, D., Bruno, M. & Ghignone, S. Gypsum: from the equilibrium to the growth shapes—theory and experiments. *Minerals* **14**, 1–20 (2024).
15. Ehlmann, B. L. & Edwards, C. S. Mineralogy of the Martian surface. *Annu. Rev. Earth Planet. Sci.* **42**, 291–315 (2014).
16. Jones, M. W. M. et al. In situ crystallographic mapping constrains sulfate precipitation and timing in Jezero crater, Mars. *Sci. Adv.* **11**, eadt3048 (2025).
17. David, G. et al. Evidence for amorphous sulfates as the main carrier of soil hydration in Gale Crater, Mars. *Geophys. Res. Lett.* **49**, e2022GL098755 (2022).
18. Vaniman, D. T. et al. Gypsum, bassanite, and anhydrite at Gale crater, Mars. *Am. Mineral.* **103**, 1011–1020 (2018).
19. Young, B. W. & Chan, M. A. Gypsum veins in Triassic Moenkopi mudrocks of southern Utah: analogs to calcium sulfate veins on Mars. *J. Geophys. Res. Planets* **122**, 2016JE005118 (2017).
20. Wu, B. et al. Landing Site Selection and Characterization of Tianwen-1 (Zhurong rover) on Mars. *J. Geophys. Res. Planets* **127**, e2021JE007137 (2022).
21. Wang, L. & Huang, J. Hypothesis of an ancient northern ocean on Mars and insights from the Zhurong rover. *Nat. Astron.* **8**, 1220–1229 (2024).
22. Bramson, A. The Amazonian climate of Mars: a cold and dry summary. *42nd COSPAR Scientific Assembly* **42**, B4–1 (2018).
23. Xiao, L. et al. Evidence for marine sedimentary rocks in Utopia Planitia: Zhurong rover observations. *Natl. Sci. Rev.* **10**, nwad137 (2023).
24. Golombek, M. P. et al. Small crater modification on Meridiani Planum and implications for erosion rates and climate change on Mars. *J. Geophys. Res. Planets* **119**, 2522–2547 (2014).
25. Li, C. et al. Layered subsurface in Utopia Basin of Mars revealed by Zhurong rover radar. *Nature* **610**, 308–312 (2022).
26. Pedersen, G. B. M. & Head, J. W. Evidence of widespread degraded Amazonian-aged ice-rich deposits in the transition between Elysium Rise and Utopia Planitia, Mars: guidelines for the recognition of degraded ice-rich materials. *Planet. Space Sci.* **58**, 1953–1970 (2010).
27. Head, J. W., Mustard, J. F., Kreslavsky, M. A., Milliken, R. E. & Marchant, D. R. Recent ice ages on Mars. *Nature* **426**, 797–802 (2003).
28. Lefort, A. et al. Observations of periglacial landforms in utopia planitia with the high resolution imaging science experiment (HiRISE). *J. Geophys. Res. Planets* **114**, E04005 (2009).
29. Ye, B. et al. Geomorphologic exploration targets at the Zhurong landing site in the southern Utopia Planitia of Mars. *Earth Planet. Sci. Lett.* **576**, 117199 (2021).
30. Graettinger, A. H., Boyd, J. & Nolan, J. A. Identification of candidate martian maars in Arena Colles and Nephentes/Amenthes with extension to maars as a proxy for past ground water/ice depths. *Icarus* **426**, 116368 (2025).
31. Russell, P. S. & Head, J. W. Elysium-Utopia flows as mega-lahars: a model of dike intrusion, cryosphere cracking, and water-sediment release. *J. Geophys. Res. Planets* **108**, 5064 (2003).
32. Ivanov, M. A., Hiesinger, H., Erkeling, G. & Reiss, D. Mud volcanism and morphology of impact craters in Utopia Planitia on Mars: Evidence for the ancient ocean. *Icarus* **228**, 121–140 (2014).
33. Brož, P. et al. An overview of sedimentary volcanism on Mars. *Earth Surf. Dyn.* **11**, 633–661 (2023).
34. Zhang, J. et al. Potential formational scenarios of the mud volcanoes in the Zhurong landing area in Utopia Planitia, observed by Tianwen-1. *Earth Planet. Sci. Lett.* **647**, 119024 (2024).
35. Pedersen, G. B. M., Head III, J. W. & Wilson, L. Formation, erosion and exposure of Early Amazonian dikes, dike swarms and possible subglacial eruptions in the Elysium Rise/Utopia Basin Region, Mars. *Earth Planet. Sci. Lett.* **294**, 424–439 (2010).
36. Broquet, A. & Andrews-Hanna, J. C. Geophysical evidence for an active mantle plume underneath Elysium Planitia on Mars. *Nat. Astron.* **7**, 160–169 (2023).

37. Taylor, S. R. & McLennan, S. *Planetary Crusts: Their Composition, Origin and Evolution* Vol. 10 (Cambridge Univ. Press, 2009).
38. Carr, M. H. & Head III, J. W. Geologic history of Mars. *Earth Planet. Sci. Lett.* **294**, 185–203 (2010).
39. Voigt, W. & Freyer, D. Solubility of anhydrite and gypsum at temperatures below 100°C and the gypsum–anhydrite transition temperature in aqueous solutions: a re-assessment. *Front. Nucl. Eng.* **2**, 1208582 (2023).
40. Ben Ahmed, S., Tlili, M. M., Amami, M. & Ben Amor, M. Gypsum precipitation kinetics and solubility in the NaCl-$MgCl_2$-$CaSO_4$-H_2O system. *Ind. Eng. Chem. Res.* **53**, 9554–9560 (2014).
41. Szynkiewicz, A., Moore, C. H., Glamoclija, M., Bustos, D. & Pratt, L. M. Origin of coarsely crystalline gypsum domes in a saline playa environment at the White Sands National Monument, New Mexico. *J. Geophys. Res. Earth Surf.* **115**, F02021 (2010).
42. Kreslavsky, M. A. & Head, J. W. Fate of outflow channel effluents in the northern lowlands of Mars: the Vastitas Borealis Formation as a sublimation residue from frozen ponded bodies of water. *J. Geophys. Res. Planets* **107**, 1–4 (2002).
43. Hiesinger, H. & Head III, J. W. Characteristics and origin of polygonal terrain in southern Utopia Planitia, Mars: results from Mars Orbiter Laser Altimeter and Mars Orbiter Camera data. *J. Geophys. Res. Planets* **105**, 11999–12022 (2000).
44. Wilson, L. & Head, J. W. Heat transfer and melting in subglacial basaltic volcanic eruptions: Implications for volcanic deposit morphology and meltwater volumes. *Geol. Soc. Spec. Publ.* **202**, 5–26 (2002).
45. Head, J. W., Wilson, L., Dickson, J. & Neukum, G. The Huygens-Hellas giant dike system on Mars: implications for Late Noachian–Early Hesperian volcanic resurfacing and climatic evolution. *Geology* **34**, 285–288 (2006).
46. Michalski, J. & Niles, P. B. Atmospheric origin of martian interior layered deposits: links to climate change and the global sulfur cycle. *Geology* **40**, 419–422 (2012).
47. Niles, P. B., Michalski, J., Ming, D. W. & Golden, D. C. Elevated olivine weathering rates and sulfate formation at cryogenic temperatures on Mars. *Nat. Commun.* **8**, 998 (2017).
48. Cotellucci, A. et al. Effect of different evaporation rates on gypsum habit: mineralogical implications for natural gypsum deposits. *Cryst. Growth Des.* **23**, 9094–9102 (2023).
49. Ayllón-Quevedo, F., Souza-Egipsy, V., Sanz-Montero, M. E. & Rodríguez-Aranda, J. P. Fluid inclusion analysis of twinned selenite gypsum beds from the Miocene of the Madrid basin (Spain). Implication on dolomite bioformation. *Sediment. Geol.* **201**, 212–230 (2007).
50. Benison, K. C. & Karmanocky, F. J. Could microorganisms be preserved in Mars gypsum? Insights from terrestrial examples. *Geology* **42**, 615–618 (2014).
51. Allwood, A. C., Burch, I. W., Rouchy, J. M. & Coleman, M. Morphological biosignatures in gypsum: diverse formation processes of messinian (~6.0 Ma) gypsum stromatolites. *Astrobiology* **13**, 870–886 (2013).
52. Pavlov, A. A., Vasilyev, G., Ostryakov, V. M., Pavlov, A. K. & Mahaffy, P. Degradation of the organic molecules in the shallow subsurface of Mars due to irradiation by cosmic rays. *Geophys. Res. Lett.* **39**, L13202 (2012).
53. Stoker, C. R. & Bullock, M. A. Organic degradation under simulated Martian conditions. *J. Geophys. Res. Planets* **102**, 10881–10888 (1997).
54. Lewis, J. M. T. et al. Organic products of fatty acid and magnesium sulfate mixtures after gamma radiolysis: implications for missions to Europa. *Astrobiology* **24**, 1166–1186 (2024).
55. Carrier, B. L., Abbey, W. J., Beegle, L. W., Bhartia, R. & Liu, Y. Attenuation of ultraviolet radiation in rocks and minerals: implications for Mars science. *J. Geophys. Res. Planets* **124**, 2599–2612 (2019).
56. Chen, Z. et al. Quality index for Martian in-situ laser-induced breakdown spectroscopy data. *Spectrochim. Acta B* **216**, 106921 (2024).
57. Wiens, R. C. et al. Pre-flight calibration and initial data processing for the ChemCam laser-induced breakdown spectroscopy instrument on the Mars Science Laboratory rover. *Spectrochim. Acta B* **82**, 1–27 (2013).
58. Zhang, Y. et al. Wavelength calibration for the LIBS spectra of the Zhurong Mars rover. *Remote Sens.* **15**, 1494 (2023).
59. Rapin, W. et al. An interval of high salinity in ancient Gale crater lake on Mars. *Nat. Geosci.* **12**, 889–895 (2019).
60. Lin, H. et al. In-flight calibration of near-infrared reflectance spectra measured by the Zhurong Mars rover. *Earth Space Sci.* **10**, e2022EA002624 (2023).
61. Ju, E. et al. Detection of allophane by the Zhurong rover indicates water-limited alteration at Utopia Planitia, Mars. *Earth Planet. Sci. Lett.* **639**, 118769 (2024).

Acknowledgements

We acknowledge the contributions of the entire Tianwen-1 mission team, with special thanks to the Ground Research and Application System (GRAS) and the Lunar and Planetary Data Release System for their invaluable support. We thank Z. Chen for his generous guidance in LIBS data analysis and helpful advice on manuscript preparation.

Author contributions

J.L. drafted the paper with suggestions and comments from all co-authors. J.L. and X.W. contributed to the conceptualization of the study. The methodology was developed by J.L., B.W., W.G. and X.H. Investigation was carried out by J.L., X.W., W.G. and X.H. J.L. and X.H. were responsible for visualization, while J.R.M. and G.Z. provided supervision for the project. All authors, including B.W., J.W.H., Z.L., Y.Q., M.-F.Z., Z.L., Z.W., C.L., X.H., A.E.W.-J., W.T., S.H., H.L. and Y.S., contributed to the writing, review and editing of the final manuscript.

Funding

This work was supported by the National Natural Science Foundation of China (grant nos. 42302264, 42441803 and 42241129 to J.L.); the National Key R&D Program of China (grant nos. 2024YFF0809800 and 2025YFF0811800 to J.L.); Dr. Stephen S.F. Hui Trust Fund 2025-26 to J.L.; the Hong Kong Research Grants Council (RGC) General Research Fund (grant nos. 17306623 and 17308625 to J.L., 17308023 to G.Z. and 17311022 to J.R.M.); the Hong Kong RGC Collaborative Research Fund (grant no. C7004-21G to J.R.M.); the Hong Kong RGC Research Impact Fund (grant no. R5043-19 to B.W.); and the Hong Kong RGC Co-funding Mechanism on Joint Laboratories with the Chinese Academy of Sciences (grant no. JLFS/P-702/24 to G.Z.).

Competing interests

The authors declare no competing interests.

Additional information

Extended data is available for this paper at https://doi.org/10.1038/s41550-026-02917-3.

Correspondence and requests for materials should be addressed to Jiacheng Liu, Joseph R. Michalski or Xiao Wang.

Peer review information *Nature Astronomy* thanks Elizabeth Rampe, Martin Voelker and the other, anonymous, reviewer(s) for their contribution to the peer review of this work.

[1]NWU–HKU Joint Center of Earth and Planetary Sciences, Department of Earth and Planetary Sciences, The University of Hong Kong, Hong Kong, China. [2]Department of Earth, Environmental and Planetary Sciences, Brown University Providence, Providence, RI, USA. [3]Planetary Remote Sensing Laboratory, Department of Land Surveying and Geo-Informatics, The Hong Kong Polytechnic University, Hong Kong, China. [4]School of Resources and Civil Engineering, Northeastern University, Shenyang, China. [5]Deparment of Earth and Planetary Sciences, The University of Hong Kong, Hong Kong, China. [6]Laboratory for Space Research, The University of Hong Kong, Hong Kong, China. [7]School of Earth Resources, China University of Geosciences, Wuhan, China. [8]Department of Earth and Planetary Sciences, McGill University, Montreal, Quebec, Canada. [9]Shandong Key Laboratory of Optical Astronomy and Solar-Terrestrial Environment, School of Space Science and Physics, Institute of Space Sciences, Shandong University, Weihai, China. [10]Center for Excellence in Comparative Planetology, Chinese Academy of Sciences, Hefei, China. [11]Key Laboratory of Earth and Planetary Physics, Institute of Geology and Geophysics, Chinese Academy of Sciences, Beijing, China. [12]China Institute of Tibetan Plateau Research, Chinese Academy of Sciences, Beijing, China. [13]CAS Key Laboratory of Mineralogy and Metallogeny/Guangdong Provincial Key Laboratory of Mineral Physics and Materials, Guangzhou Institute of Geochemistry, Chinese Academy of Sciences, Guangzhou, China. [14]CAS Center for Excellence in Deep Earth Science, Guangzhou, China. [15]State Key Laboratory of Continental Evolution and Early Life, NWU–HKU Joint Centre of Earth and Planetary Sciences, Department of Geology, Northwest University, Xi'an, China. ✉e-mail: jcliu01@hku.hk; jmichal@hku.hk; wangfuyu@hku.hk

https://doi.org/10.1038/s41550-026-02917-3

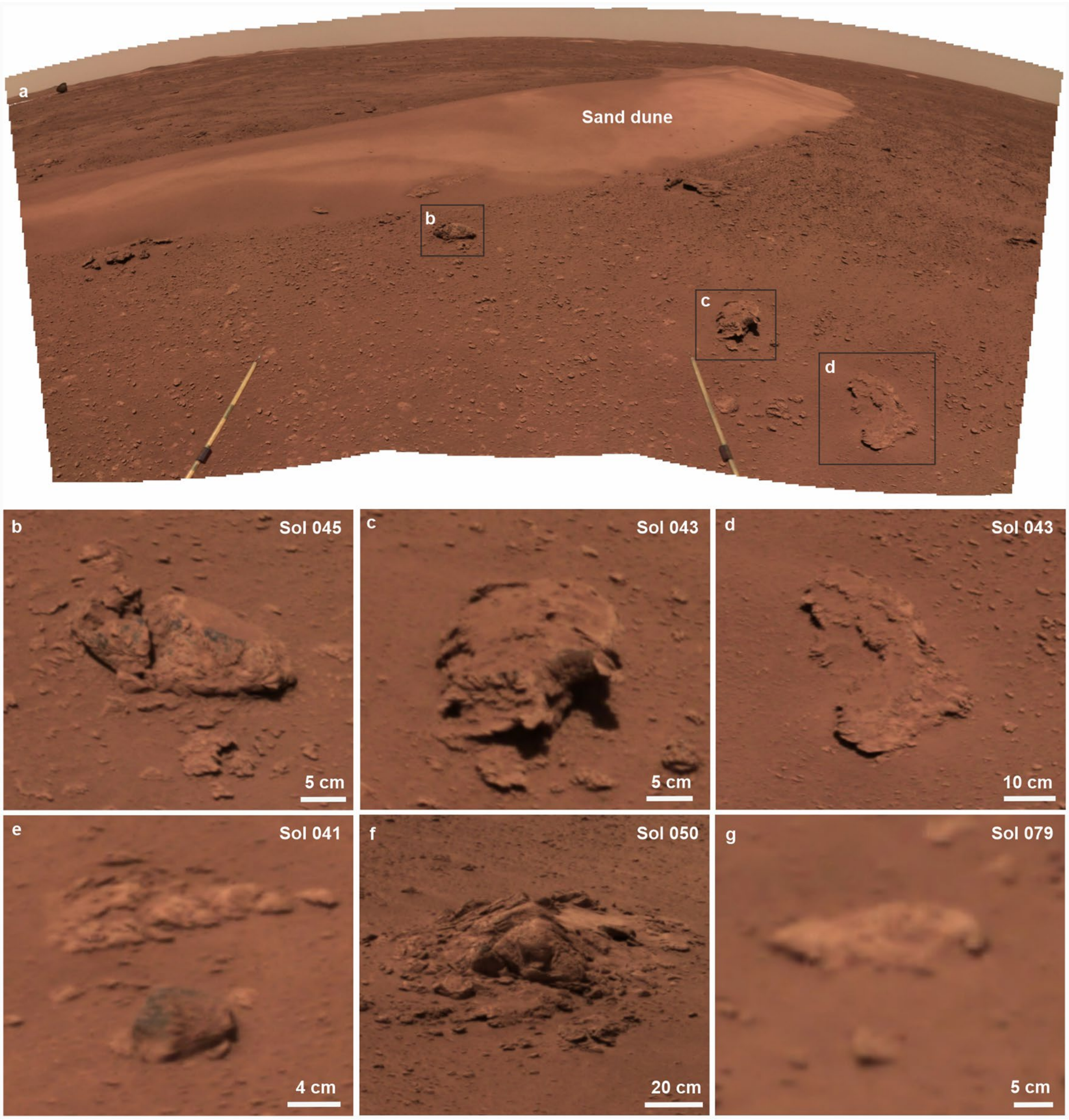

Extended Data Fig. 1 | The platy rocks experienced strong aeolian abrasion. **a** A transverse aeolian ridge covering the platy rocks rich in hydrous minerals. **b-g** Bright-toned platy rocks captured at different locations and times along the traverse (Sol 045 (**b**); Sol 043 (**c**, **d**); Sol 041 (**e**); Sol 050 (**f**); Sol 079 (**g**)) by the Navigation and Terrain Cameras (NaTeCams). The bright-toned platy rocks in **c** and **d** are observed at different positions during the same Sol.

 https://doi.org/10.1038/s41550-026-02917-3

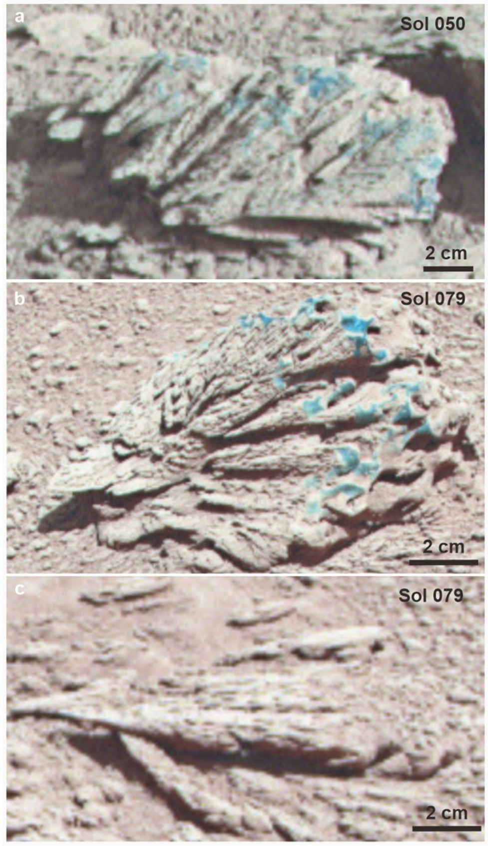

Extended Data Fig. 2 | Sharp-angled rock fragments with prominent intercrystalline voids. a-**c** Sharp-angled rock fragments captured at different locations and times along the traverse (Sol 050 (**a**); Sol 079 (**b**, **c**)) by the MSCam. The sharp-angled rock fragments in **b** and **c** are observed at different positions during the same sol.

 https://doi.org/10.1038/s41550-026-02917-3

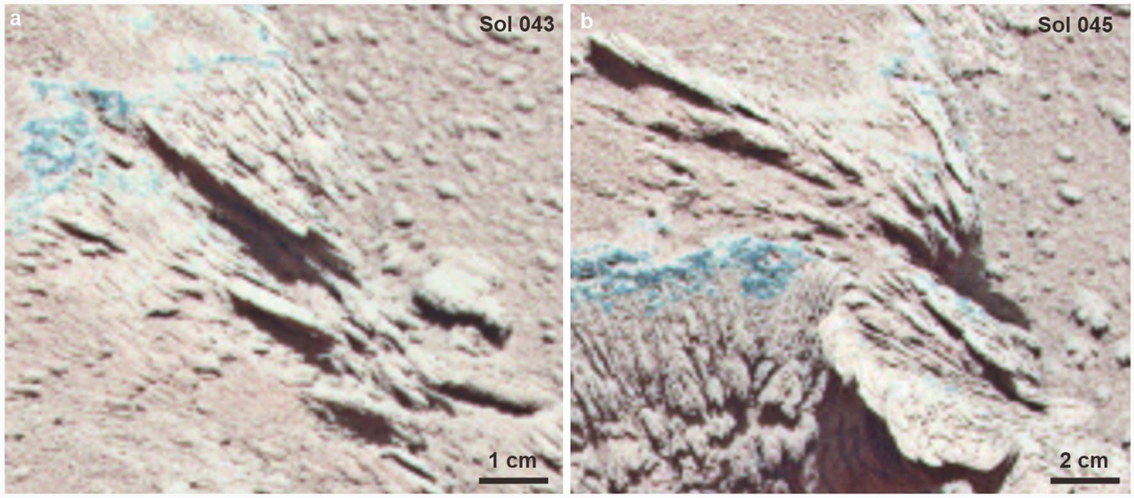

Extended Data Fig. 3 | Tabular crystals of gypsum selenite at the Zhurong landing site. Tabular crystals of gypsum selenite captured at different locations and times along the traverse (Sol 043 (**a**); Sol 045 (**b**)) by the MSCam.

 https://doi.org/10.1038/s41550-026-02917-3

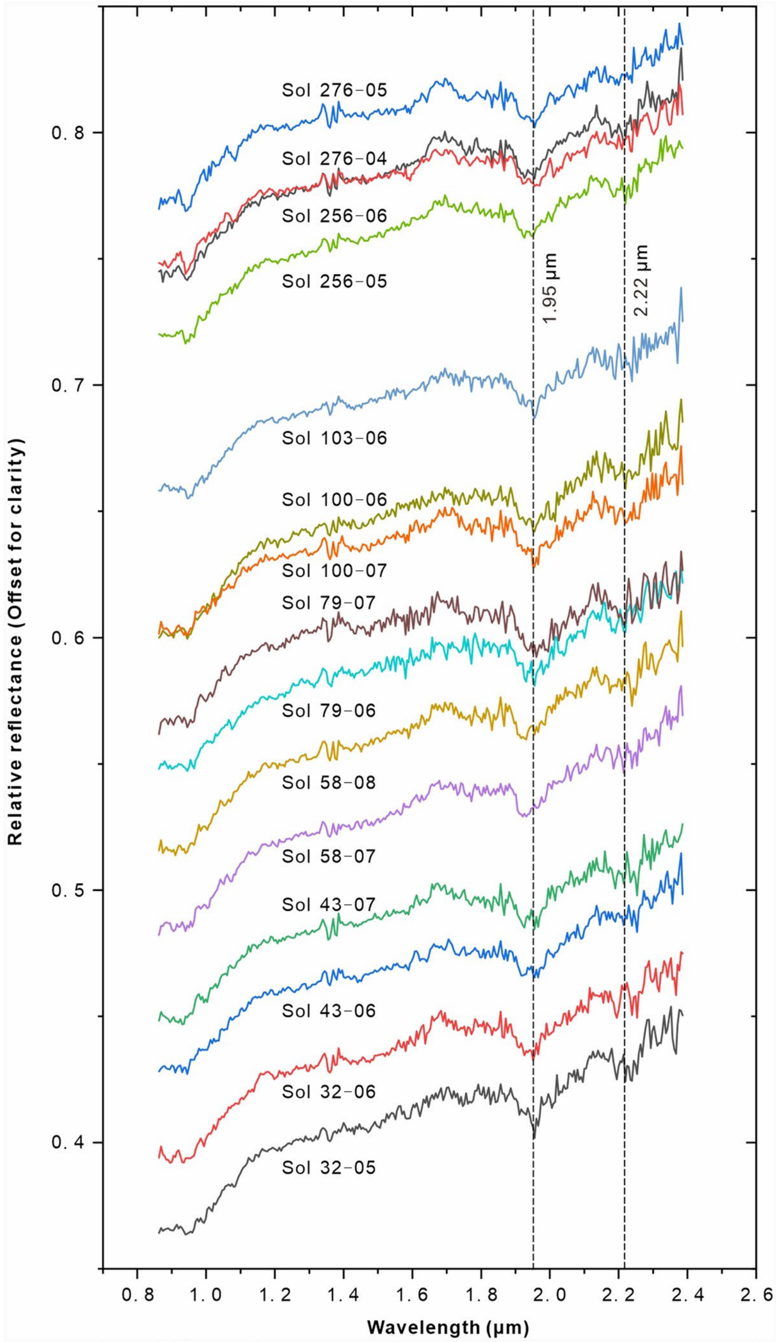

Extended Data Fig. 4 | The reflectance spectra of platy rocks collected by Zhurong. These reflectance spectra display a similar overall shape and diagnostic absorption features at ~1.95 and ~2.22 μm.

https://doi.org/10.1038/s41550-026-02917-3

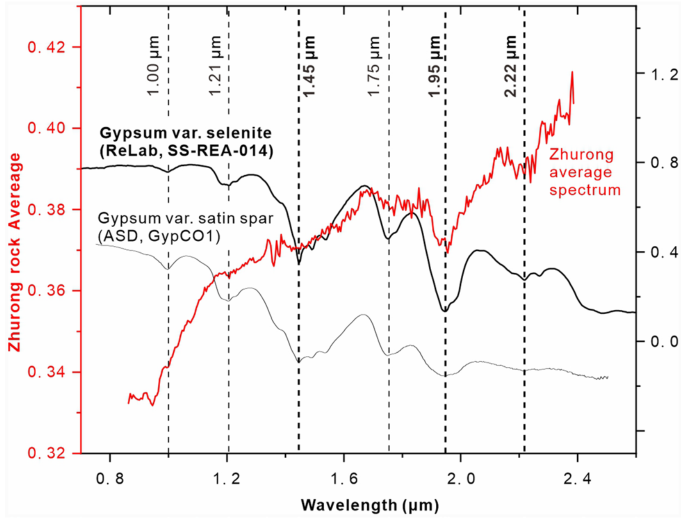

Extended Data Fig. 5 | The comparison between the average spectrum of the Zhurong platy rocks and the gypsum selenite reference spectrum. The major spectral absorptions (1.00, 1.21, 1.75, 1.95, and 2.22 µm) characteristic of gypsum selenite are all present in the average spectrum of the Zhurong platy rocks.

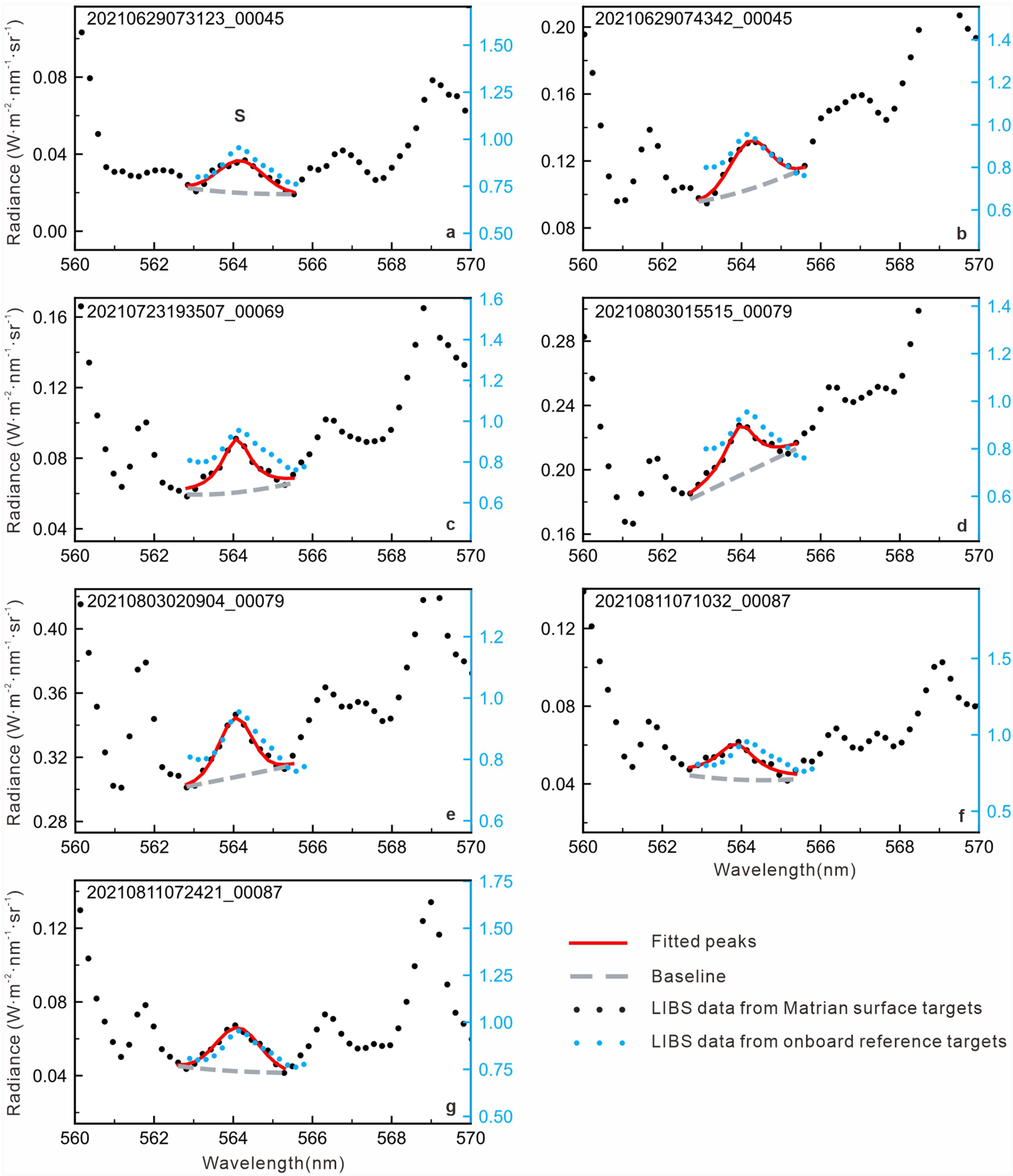

Extended Data Fig. 6 | The LIBS detection of sulfur in platy rocks. a-g, The LIBS detections of sulfur at different locations and times along the traverse (Sol 045 (**a**, **b**); Sol 069 (**c**); Sol 079 (**d**, **e**); Sol 087 (**f**, **g**)) by MarSCoDe LIBS. The sulfur in **a** and **b**, **d** and **e**, as well as **f** and **g** are detected at different positions during the same Sols.

https://doi.org/10.1038/s41550-026-02917-3

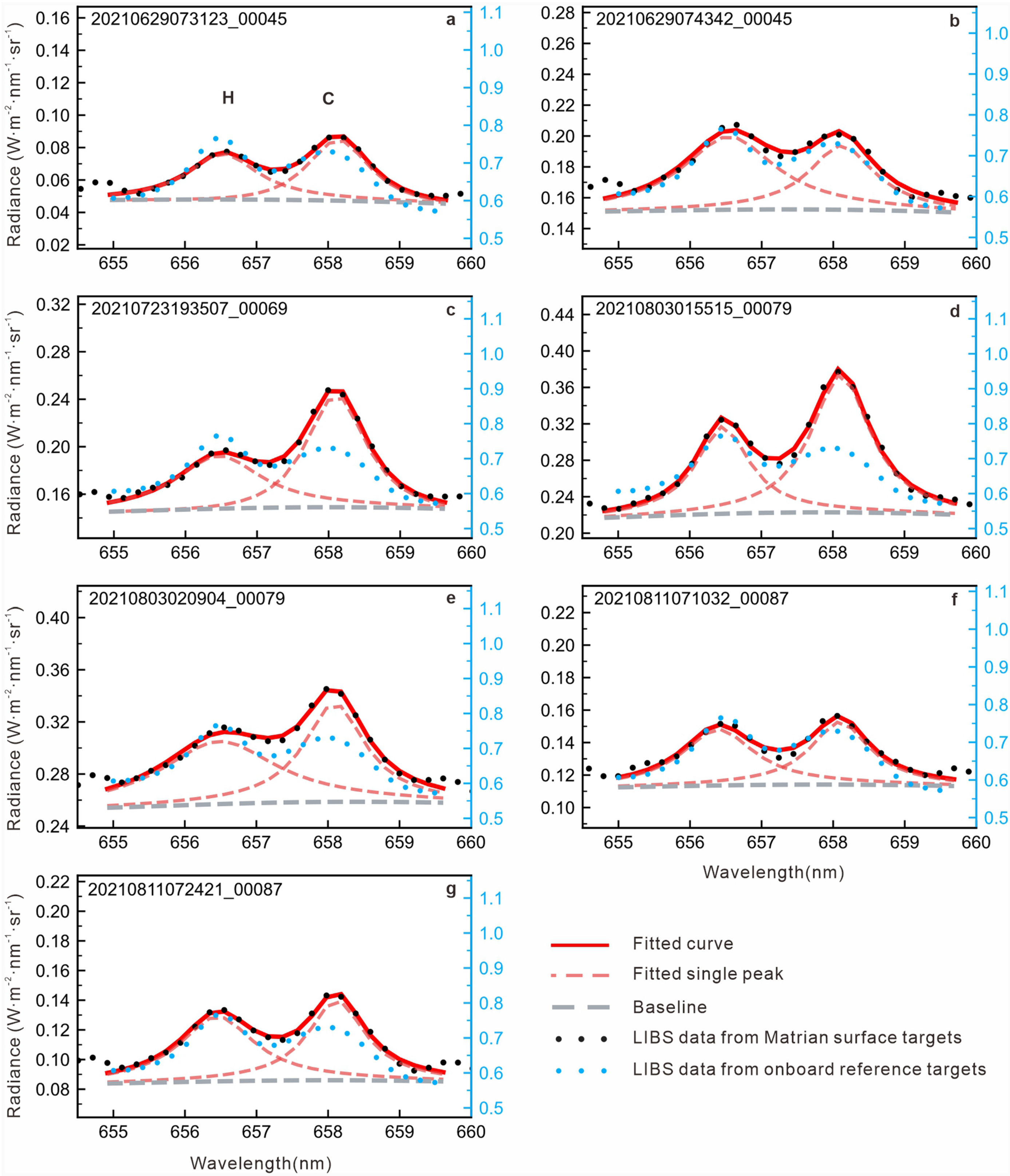

Extended Data Fig. 7 | The LIBS detection of H in platy rocks. **a**-**g**, The LIBS detections of H at different locations and times along the traverse (Sol 045 (**a**, **b**); Sol 069 (**c**); Sol 079 (**d**, **e**); Sol 087 (**f**, **g**)) by MarSCoDe LIBS. The sulfur in **a** and **b**, **d** and **e**, as well as **f** and **g** are detected at different positions during the same Sols.

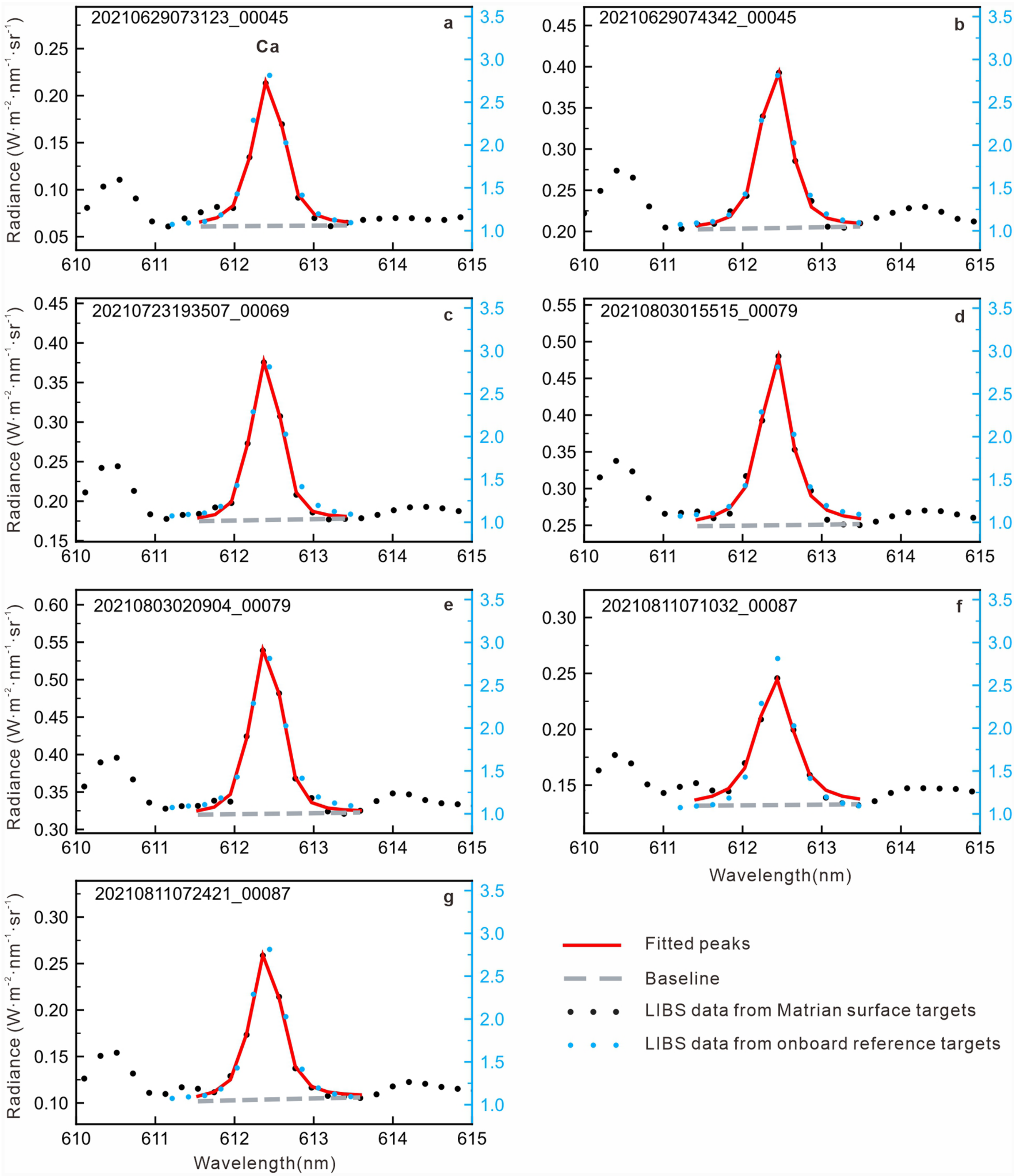

Extended Data Fig. 8 | The LIBS detection of Ca in platy rocks. a-g, The LIBS detections of Ca at different locations and times along the traverse (Sol 045 (**a**, **b**); Sol 069 (**c**); Sol 079 (**d**, **e**); Sol 087 (**f**, **g**)) by MarSCoDe LIBS. The Ca in **a** and **b**, **d** and **e**, as well as **f** and **g** are detected at different positions during the same Sols.

 https://doi.org/10.1038/s41550-026-02917-3

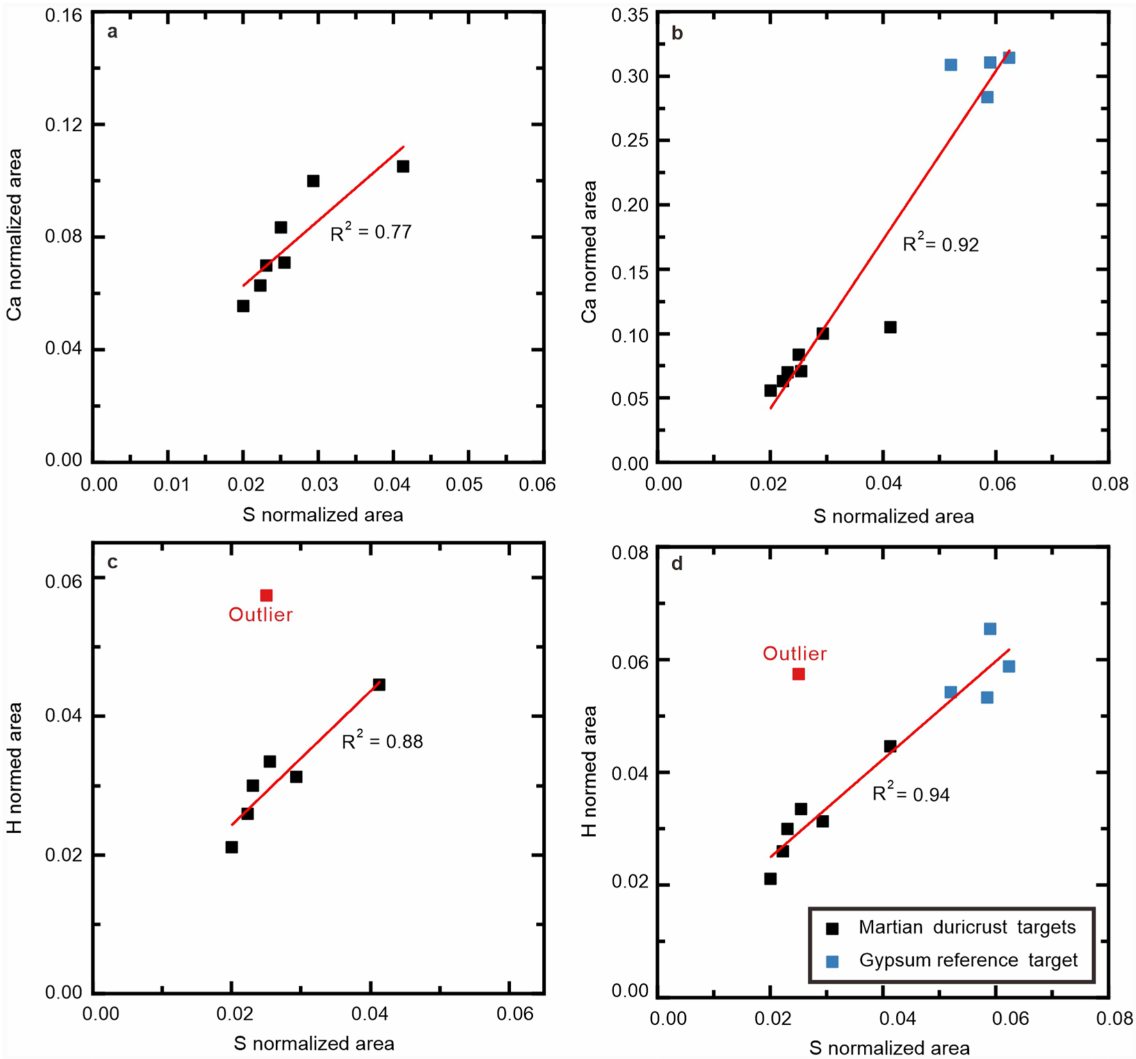

Extended Data Fig. 9 | The positive correlation between normalised areas of diagnostic peaks of S, H and Ca in rocks and gypsum reference onboard Zhurong. **a** The positive correlation between the normalised areas of S and Ca of platy rocks. **b** The positive correlation between the normalised areas of S and Ca of platy rocks and gypsum reference. **c** The positive correlation between the normalised areas of S and H of platy rocks. **d** The positive correlation between the normalised areas of S and H of platy rocks and gypsum reference. The outlier is rich in Si, which might be caused by surface hydrated silica or allophane[4,61], which would contribute additional H.

https://doi.org/10.1038/s41550-026-02917-3

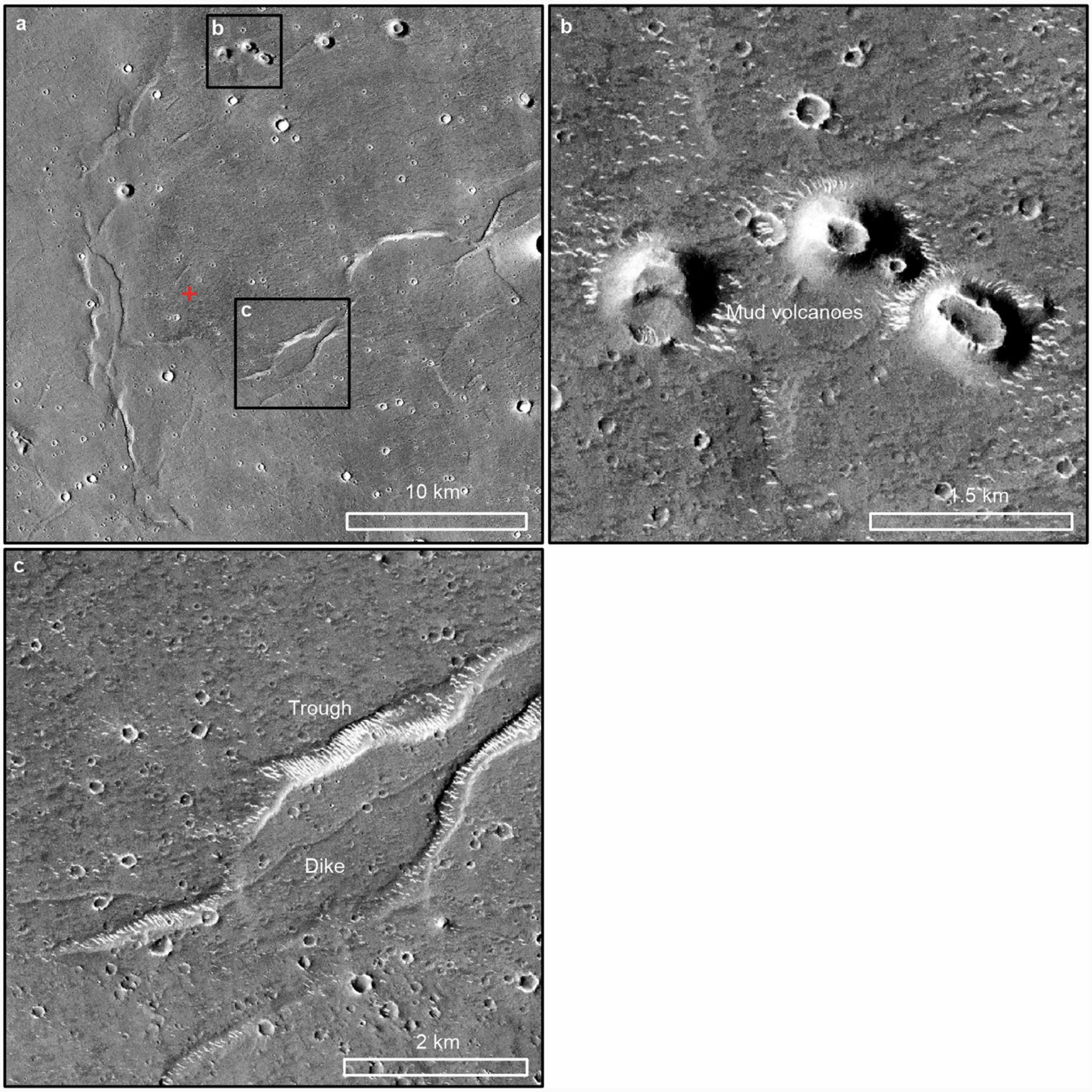

Extended Data Fig. 10 | Distinctive landforms associated with volatiles in the Zhurong landing region. a The CTX image of the Zhurong landing region. The CTX images of mud volcanoes (**b**), and dike and troughs (**c**). Red cross is the landing site of the Zhurong rover (25.066°N, 109.925°E).